Degenerate Electron-Doping in Two-dimensional Tungsten
Diselenide with a Dimeric Organometallic Reductant

Rui Guo¹, Qiang Li², Yue Zheng^{3,4}, Bo Lei^{3,4}, Haicheng Sun¹, Zehua Hu^{3,4}, Jialin Zhang^{1,3}, Li Wang⁵, Elena Longhi⁶, Stephen Barlow⁶, Seth R. Marder⁶, Jinlan Wang^{2,7}, Wei Chen^{1,3,8,9}

¹Department of Chemistry, National University of Singapore, 117543, Singapore

²School of Physics, Southeast University, Nanjing, 211189, P.R. China

³Department of Physics, National University of Singapore, 117542, Singapore

⁴Center for advanced 2D materials, National University of Singapore, 117546, Singapore

⁵Institute for Advanced Study and Department of Physics, Nanchang University, Nanchang, 330031, P.R. China

⁶Center for Organic Photonics and Electronics and School of Chemistry and Biochemistry, Georgia Institute of Technology, Atlanta, Georgia 30332, USA

⁷Synergetic Innovation Center for Quantum Effects and Applications (SICQEA), Hunan Normal University, Changsha, 410081, P.R. China

⁸National University of Singapore (Suzhou) Research Institute, Suzhou, 215123, P.R. China

⁹Joint School of National University of Singapore and Tianjin University, International Campus of Tianjin University, Binhai New City, Fuzhou, 350207, P. R. China

*E-mail: jlwang@seu.edu.cn (JL Wang)

*E-mail: phycw@nus.edu.sg (W Chen)

Abstract: The large Schottky barriers formed at metal-semiconductor junctions severely limit the development of transition metal dichalcogenide (TMDC) based ultrathin electronics and optoelectronics. Various approaches to create Ohmic contacts at TMDC and metal interface have been developed, including contact phase engineering, contact

doping, buffer layer engineering and contact integration engineering. Here we report degenerate electron doping of mono- and bi-layer tungsten diselenide (WSe₂) by a molecular organometallic donor, [RuCp*(mes)]₂. *In-situ* evaporation of [RuCp*(mes)]₂ molecules onto WSe₂ field-effect transistors in vacuum leads to a remarkably diminished gate dependence of the transport property and a large enhancement of electrical conductance by five orders of magnitude, implying the great potential of this doping approach in tuning the Schottky barrier for TMDC devices. The interfacial electronic structure at the WSe₂-dopant interface was revealed through the combination of *in-situ* photoelectron spectroscopy investigations and theoretical calculations. Moreover, the doped device is found to be robust in oxygen and nitrogen atmosphere and also moderately stable in humid air, which is favorable in device applications.

Keywords: degenerate doping, density functional calculations, interfaces, stability, tungsten diselenide

1. Introduction

Transition metal dichalcogenides (TMDCs) are representative two-dimensional (2D) materials whose properties vary depending on the combination of metal and chalcogen elements [1-3]. The presence of a bandgap in TMDCs renders them more versatile than the gapless graphene in logic electronics and also more compatible with optoelectronic applications [2-4]. However, a Schottky barrier (SB) is usually formed at the interface between TMDC and metal contacts, which is a significant impediment to the further optimization of their device performance [5,6]. Ideally, the SB can be minimized by selecting proper metal contacts on the basis of energy level alignment predicted by

Schottky-Mott rule [7-9]. However, the inevitable presence of the Fermi-level pinning effect induced by surface states and metal induced gap states, along with interfacial chemical bonding often leads to the failure of theoretical prediction [5,10-13]. In addressing the SB problem, various attempts have been reported [5,6,14]. Very recently, Liu et al. reported a contact integration approach to realize van der Waals metalsemiconductor junctions [5]. By dry transferring pre-patterned metal films in a laminating process onto TMDC channels, the interface created is free from apparent chemical disorder such as those arising from defects, metal diffusion, interface bonding, or strain. The interfacial energy level alignment obeys to the Schottky-Mott rule well and a low SB for both electron and hole can be achieved by choosing metal electrode with matching work function. Another strategy is to exploit graphene instead of conventional metals as contacts or insert graphene as buffer layers between the channel and contact. This strategy has been intensively investigated on MoS₂ [14-16]. Due to the limited electronic density of states (DOS), the Fermi level of graphene can be readily tuned under electrostatic gating or chemical doping and hence the contact barrier for both electron and hole can be reduced. SB can also be effectively minimized by inducing local semiconducting phase to metallic phase transition of TMDC intimate to metal contact [6,17,18]. One of the pioneering studies on phase engineering was reported by Kappera et al. [6]. A solution of n-butyl lithium was used to donate electrons into the 2H-MoS₂ and induce phase transition of MoS₂ into 1T metallic phase. The induced 1T-MoS₂/gold contacts exhibit contact resistance of only $0.2 \sim 0.3 \text{ k}\Omega$ µm, much smaller than the $1 \sim 10$ $k\Omega$ µm contact resistance at the 2H-MoS₂/gold interface.

Surface charge transfer doping is another effective approach to reduce SB as it can modulate the charge carrier density while retaining the intrinsic lattice structure [19-22]. The capability of spatial confinement of this technique makes it possible to realize localized doping of channel material at and/or close to the contact region. Compared with other common dopants for surface charge transfer doping on TMDCs, for instance, alkali metals [23,24], organic molecular dopants stand out for their relatively high air-stability and feasibility to be processed in either solution or vacuum conditions [25-27]. However, there are still few stable yet strong molecular n-type dopants [27-30]. Recently, molecular dopants consisting of dimers of either 19-electron sandwich compound or of organic radicals have been reported to possess moderate air-stability and can effectively realize ndoping in organic semiconductors as well as surfaces and low-dimensional materials [26,31-35], including few-layer TMDCs [30,32,36]. However, to date the use of dimers to dope TMDCs have been limited to solution processing, in which the interfaces established are not sufficiently clean to understand the fundamental interaction between TMDCs and the dopants. Here we use an example of such dimer molecules: mesitylene pentamethylcyclopentadienyl ruthenium dimer, [RuCp*(mes)]₂, processed by vacuum evaporation to achieve degenerate electron doping in exfoliated mono- and bi-layer tungsten diselenide (WSe₂). The electrical conductance of a typical WSe₂ field-effect transistor (FET) can be improved by five orders of magnitude, together with good stability against oxygen, demonstrating great potential of this doping manner in tuning SB height for TMDC devices.

2. Results

The dimeric compound [RuCp*(mes)]₂, as shown in **Figure 1**a, is relatively air-stable but its dissociated product, the monomer form [RuCp*(mes)] is highly reducing. The highest occupied molecular orbital (HOMO) position relative to the vacuum level for [RuCp*(mes)]₂ is ca. –3.7 eV while for [RuCp*(mes)] [to be more specific, singly occupied molecular orbital (SOMO) here as the monomer is indeed an odd-electron compound] is only ca. –2.1 eV [31] (Figure 1b). The ionization energy for [RuCp*(mes)] is, therefore, 1.6 eV lower than [RuCp*(mes)]₂. Although the direct dissociation of [RuCp*(mes)]₂ from dimer to monomer is energetically unfavourable [31,37], once the dimer undergoes one-electron oxidation, either through exergonic or moderately endergonic electron transfer (estimated to be moderately exergonic reaction in the case of WSe₂ as shown in Figure 1b), the central C-C bond of the dimer cation quickly breaks to form one monomer cation and another monomer [37], the latter being able to undergo exergonic electron transfer to the underlying WSe₂.

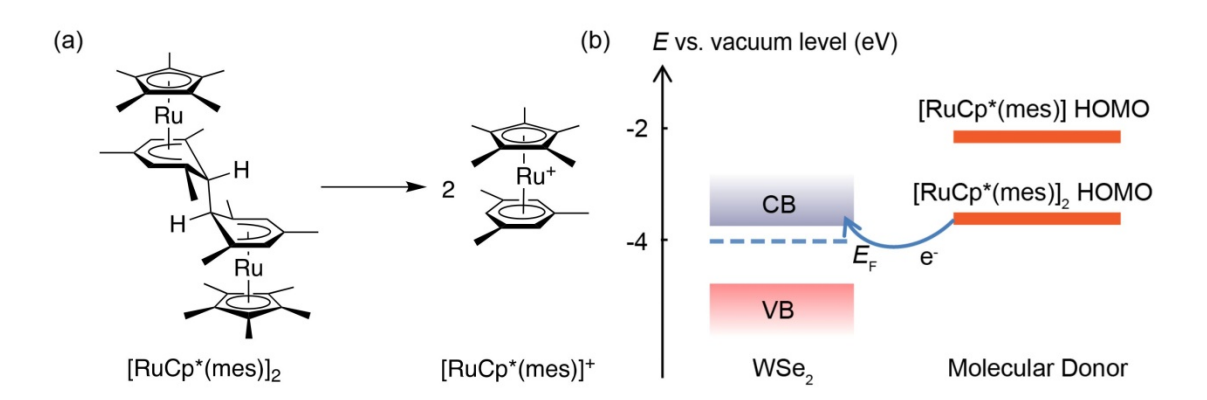


Figure 1. (a) Chemical structures of the dimer molecule $[RuCp*(mes)]_2$ and its oxidation product, the cationic monomer. (b) Energy level alignment of WSe₂ and molecular donors. E_F : Fermi level; CB: conduction band; VB: valence band.

In line with our assumption, efficient degenerate n-doping of WSe₂ FETs were achieved via vacuum deposition of [RuCp*(mes)]₂ on the WSe₂ surface (**Figure 2**). The device characterizations of a representative bilayer WSe₂ FET are shown in Figure 2a, 2b, 2c and 2d. The bilayer nature of the exfoliated WSe2 flake configured for the device was confirmed by Raman spectrum [38,39] and an atomic force microscope (AFM) height profile (Figure 2a), as well as its photoluminescence (PL) spectrum (Figure S1). The logarithmic plot of the transfer curve (Figure 2c) clearly demonstrates that the holedominant ambipolar behaviour of pristine WSe₂ device is converted into one exhibiting electron-dominant characteristics with a weak gate dependence upon the in-situ deposition of only 0.1 nm [RuCp*(mes)]₂. The electron mobility increases from 3.4×10^{-1} ² cm² V⁻¹ s⁻¹ to 9.6 cm² V⁻¹ s⁻¹ after the deposition of a 0.8 nm thickness of the molecular donor. The charge carrier (electron) density in the doped WSe_2 calculated at $V_g = 40 \text{ V}$ also increases and reaches a saturation value of 2.5×10^{12} cm⁻². We propose that the electrons transferred from the molecular donor first fill the electron traps within the bandgap of WSe₂ and the increased electron density further provides better screening of these defects, leading to an substantial enhancement of the electron mobility (see also Figure S2) [40]. Further increasing the molecular donor amount does not lead to an obvious enhancement of charge carrier mobility and concentration. The electrical conductance ($G = I_{sd}/V_{sd}$) at zero gate voltage was calculated and plotted versus the nominal thickness of the dopant layer in Figure 2d. A conductance enhancement of five orders of magnitude was observed, i.e, from $5.4 \times 10^{-6} \,\mu\text{S}$ to a saturated conductance of 0.65 µS. The degenerate transport behavior and dramatic conductance enhancement were also observed in monolayer WSe₂ devices (Figure 2e and 2f, more discussion can be

found in supporting information). We note that for monolayer WSe₂, the on current of the pristine device is over one order of magnitude lower than the bilayer counterparts. This is reasonable considering the relatively larger bandgap and thus larger band offset of monolayer WSe₂, which leads to higher Schottky barrier for the transport of charge carriers [41]. A statistical summary of the distribution of electrical conductance enhancement for all the 2D devices measured (>5) is also given in Figure S5. In addition, device characteristics under varying temperatures reveal significant reduction (more than 80%) of SB heights extracted at WSe₂/metal interface after deposition of the dopant (Figure S6). In-situ Raman and PL measurements were conducted on WSe2 before and after modification. As shown in the Raman spectra (Figure S7), neither obvious shift of the characteristic peaks, i.e., E_{2g}^1 and A_{1g} , nor the appearance of new features was observed after the dopant deposition. The crystal structure of WSe₂ therefore is well retained with molecular modification. As for PL spectra in Figure S8, the overall PL intensity was quenched while the ratio of the two components, trion peak/exciton peak, increased with increasing amount of molecule. This evolution is reasonable considering the electrons injection into WSe₂ and is also consistent with previous report on TMDCs doped by a molecular dopant with a similar structure [36].

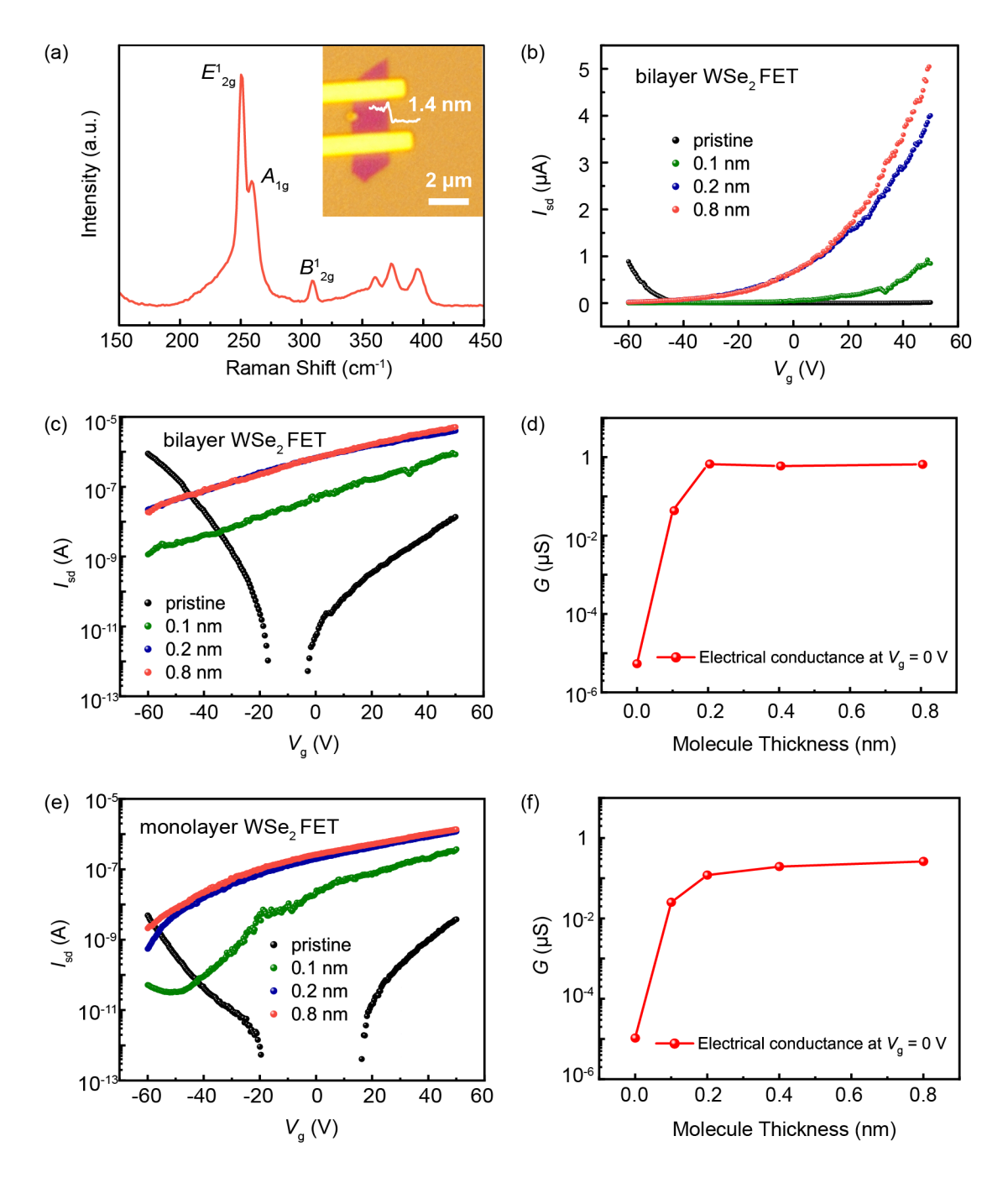


Figure 2. Characterizations of WSe₂ FETs functionalized with $[RuCp^*(mes)]_2$. (a) Raman spectrum, optical image, and AFM height profile of a bilayer WSe₂ flake configured for the two-terminal device. (b) Linear and (c) logarithmic plot of transfer curves of the WSe₂ device shown in (a) ($V_{sd} = 1$ V) with increasing nominal molecular thickness from 0 to 0.8 nm. (d) Thickness dependent electrical conductance evolution of the bilayer WSe₂ device at zero gate voltage. (e) Logarithmic plot of transfer curve for a monolayer WSe₂ FET ($V_{sd} = 1$ V) with increasing nominal molecular thickness. (f) Thickness dependent electrical conductance evolution of the monolayer WSe₂ device at zero gate voltage.

To further study the interfacial charge transfer mechanism between [RuCp*(mes)]₂ and WSe₂, in-situ ultraviolet photoelectron spectroscopy (UPS) and x-ray photoelectron spectroscopy (XPS) measurements were conducted. In Figure 3a, the surface work function of WSe₂ (determined from the linear extrapolation of the secondary electron cutoff) was significantly reduced from 4.1 eV at pristing to a saturation of 2.4 eV after the deposition of an effective dopant film thickness of 0.4 nm. Such large decrease of surface work function is expected to arise from the strong interfacial electron transfer from the adsorbed [RuCp*(mes)]₂ to the underlying WSe₂, both due to filling of the WSe₂ band structure and due to the resultant interfacial dipole; this is also consistent with the degenerate electron-doping results revealed by the *in-situ* device measurements in Figure 2. Meanwhile, a sharp peak near the Fermi level appears even after the deposition of 0.1 nm film of dopants. The peak intensity gradually increases and approaches its maximum at 0.4 nm coverage, then steadily attenuates and finally disappears at 1.3 nm. The possibility of chemical bond formation between WSe₂ and dopant leading to this feature is excluded by the absence of new features in the core level W 4f and Se 3d spectra during the *in-situ* deposition of [RuCp*(mes)]₂ on WSe₂ (Figure S9). The origin of this feature is discussed further below in the context of DFT calculations. It has been mentioned above that the formation of the monomer [RuCp*(mes)] with low oxidation potential and strong electron doping capability is initiated by the electron transfer between WSe₂ and [RuCp*(mes)]₂. When the molecular thickness increases beyond one monolayer (~0.4 nm assuming a molecular configuration with the metal-ligand axis normal to the surface [42]), the [RuCp*(mes)]₂ on top of this monolayer is no longer in direct physical contact with the underlying WSe₂, which, together with the large interfacial dipole, hinders interfacial charge transfer and leaves the [RuCp*(mes)]₂ dimers intact. This is consistent with the saturation of the work function observed in the UPS data at around this thickness (Figure 3a). The thickness dependent Ru 3d core level spectra in Figure 3b also agrees with this picture: when molecular thickness is only 0.4 nm, only signals attributable to the monomeric cation (Ru^{II+δ+} 3d) exists; while at higher thickness, both signals attributable to monomeric cation and excess intact dimers (Ru^{II} 3d) coexist [43]. A schematic illustration of the interfacial charge transfer process is presented in Figure 3c. We note that in Figure 3b, the C 1s peak shifts to higher binding energy by 0.3 eV at higher molecular thickness, which is attributed to the reduction of substrate enhanced screening effect of the C 1s core hole [44].

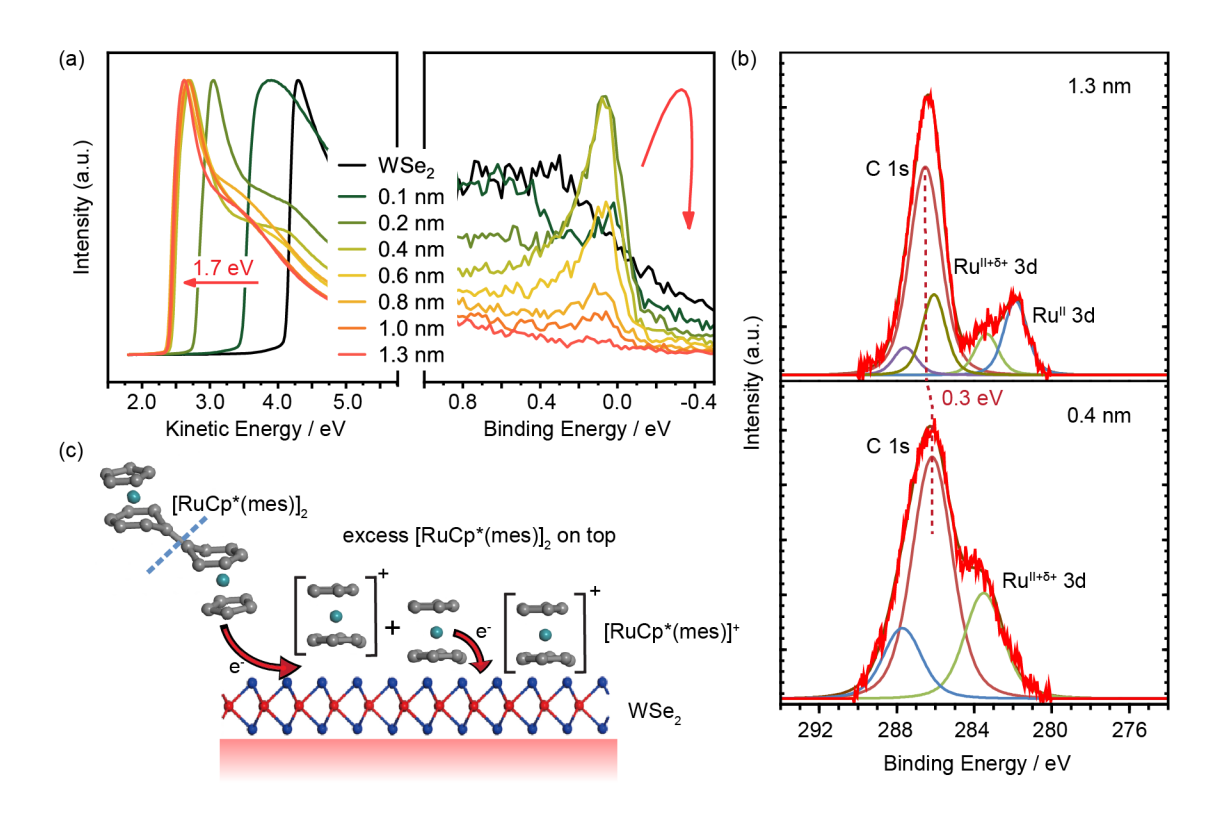


Figure 3. (a) UPS spectra at low kinetic energy region (secondary electron cut off, left) and close up spectra near the Fermi level region (right) of WSe₂ with increasing nominal molecular thickness from 0 to 1.3 nm. (b) Peak fitting of core level spectra of C 1s and Ru 3d region for [RuCp*(mes)]₂ deposited on WSe₂, with nominal molecular thickness of

1.3 nm (top) and 0.4 nm (bottom), respectively. (c) A schematic illustration of the interfacial charge transfer process (CH₃ groups excluded for simpilicity).

We also found out the modified device demonstrates excellent stability in dry O_2 and N_2 atmosphere and also relatively good stability in air. As shown in **Figure 4**a, after exposing the bilayer WSe₂ FET device coated with 1.2 nm [RuCp*(mes)]₂ to pure O_2 for 20 hours, the source-drain current closely resembles the curve before exposure with only a slight drop of no more than one order of magnitude. Figure 4b plots the evolution of electrical conductance at zero gate voltage extracted from transfer curves. We observed this conductance decreases slightly upon contact with O_2 and then remains stable with increasing exposure time, illustrating the high endurance of the n-doped WSe₂ in O_2 . Devices were more stable in N_2 (Figure 4c), but after ten-hour exposure to air with $60{\sim}80\%$ humidity, the electrical conductance at zero gate voltage in Figure 4d only decreases by less than two orders of magnitude, revealing a relatively good air stability. The transfer curves of WSe₂ device before and after exposure to N_2 and air, respectively, are given in Figure S10.

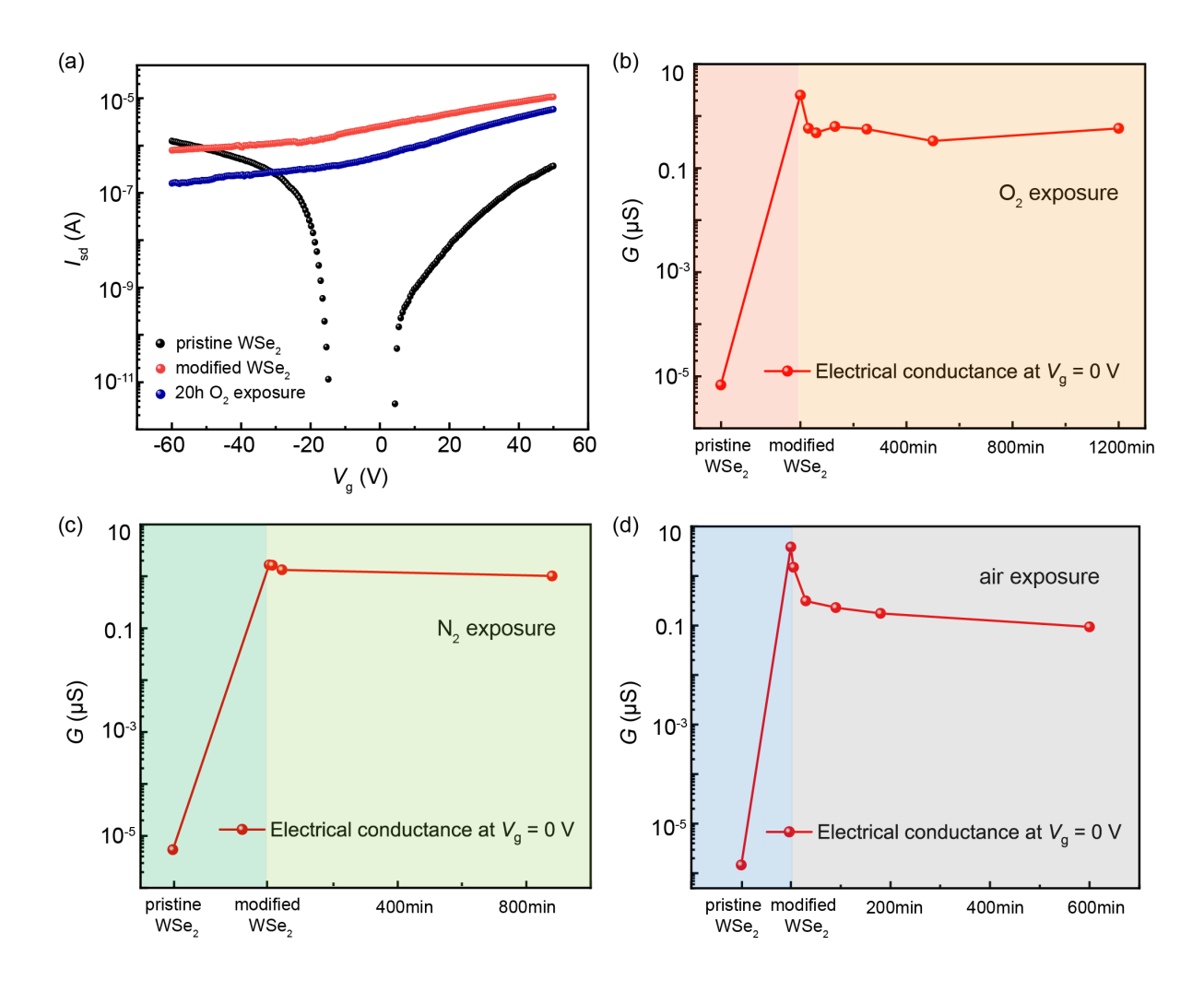


Figure 4. Stability investigation of WSe₂ FET functionalized with [RuCp*(mes)]₂. (a) The comparison of transfer curves in logarithmic scale at $V_{\rm sd} = 1$ V of the pristine bilayer WSe₂ device, the same device modified by [RuCp*(mes)]₂ and then *in-situ* exposed to O₂ for 20 h. Electrical conductance evolution of bilayer WSe₂ devices at zero gate voltage before and after surface funtionalization and then exposed to (b) O₂, (c) N₂, and (d) air.

Density functional theory (DFT) calculations were employed to gain further insight into the interfacial interaction as well as the possible origin of the state responsible for the features near the Fermi level in Figure 3a. The simulations were conducted on the system comprising one monomer [RuCp*(mes)] and a 4×4 super cell of monolayer or bilayer WSe₂. As the bottom layer in bilayer WSe₂ has little influence on the interaction between molecule and the top layer, here we only present DFT results on monolayer for a better

visual interpretation. DFT results on bilayer WSe₂ can also be found in Figure S11. **Figure 5**a and 5b show the calculated band structure of the pristine monolayer WSe₂ and the [RuCp*(mes)] functionalized monolayer WSe₂. We note that the adoption of different dispersion correction methods has no significant influence in analyzing the electronic properties of the hybrid system (Figure S12). The partial charge density analysis (insert in Figure 5b) reveals that no chemical bond formed at the interface, consistent with XPS results. The charge transfer process is further illustrated by charge density difference between [RuCp*(mes)]-WSe₂ complex and isolated components (Figure 5c) and by Bader charge analysis, which indicates 0.4 e⁻ is transferred from one [RuCp*(mes)] monomer to the underlying WSe₂ monolayer, resulting in the partial occupation of conduction bands around Γ point (monolayer WSe₂) or M-K point (bilayer WSe₂, Figure S11). The DFT analysis can explain the origin of the interface state observed in UPS as arising from the partially occupied conduction band of WSe₂ and the partially depleted SOMO-derived states of [RuCp*(mes)] pinned at the Fermi level (Figure 5d).

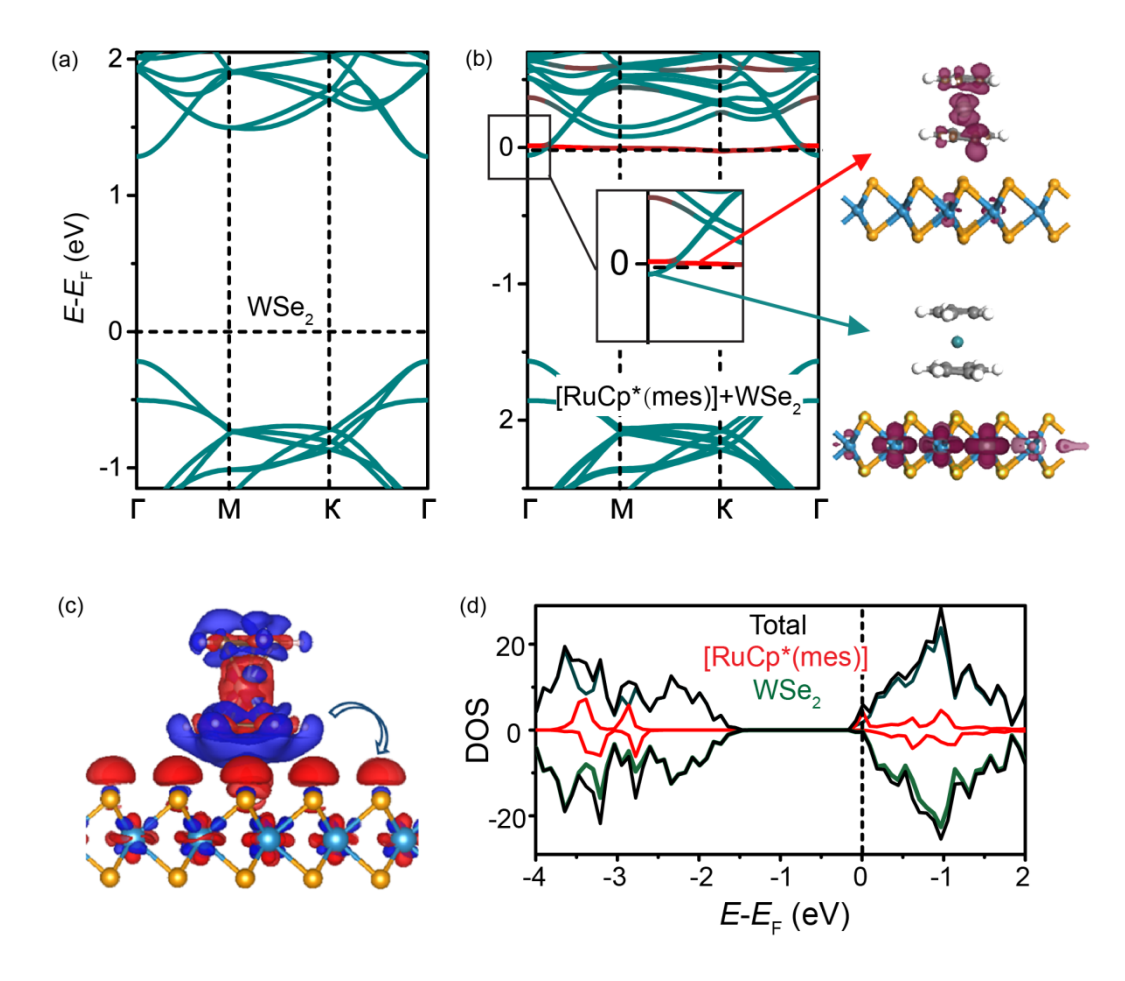


Figure 5. DFT calculated interface structure between WSe₂ and [RuCp*(mes)]. Band structures of (a) pristine monolayer WSe₂ and (b) monolayer WSe₂ with one [RuCp*(mes)] monomer. The Fermi level is set to zero. Insert in panel (b): zoom-in of the region near Fermi level at Γ point and the corresponding partial charge density plots of the two bands. (c) Charge density difference between [RuCp*(mes)]-WSe₂ complex and isolated components, where the isovalue is set to be 0.0006 e/Å^3 . Red and blue colors represent charge accumulation and depletion region, respectively. The energy change associated with adsorption of the [RuCp*(mes)] onto WSe₂ is calculated to be -0.23 eV per molecule. (d) DOS of the [RuCp*(mes)]-WSe₂ system.

3. Conclusion

In summary, we report an effective and nondestructive doping method to achieve degenerate electron doping of monolayer and bilayer WSe₂ by *in-situ* evaporating molecular dopant, [RuCp*(mes)]₂. The electrical conductance in WSe₂ can be enhanced by five orders of magnitude on average after the surface functionalization of only 0.2 nm

[RuCp*(mes)]₂. Gas exposure tests in a well-controlled manner show that the doped devices possess high stability in oxygen and nitrogen atmospheres, as well as relatively good stability in air. Our approach demonstrates great potential for contact doping engineering to significantly reduce the contact resistance (or SB) at the TMDC/metal interface, and further optimize the performance of TMDC based electronic and optoelectronic devices.

4. Experimental Section

WSe₂ device fabrication: The flake of WSe₂ was mechanically exfoliated from bulk WSe₂ crystals (as purchased from hq-graphene) by a scotch tape and then transferred onto degenerately p-type doped silicon wafers with 300 nm SiO₂ coating. Once the position of exfoliated flake was located using high-resolution microscope (Nikon Eclipse LV100D), photoresist PMMA was immediately spin coated onto the sample to protect the flake against air. The source and drain electrodes were precisely patterned on the flake via conventional e-beam lithography technique, followed by thermal evaporation of Ti (20 nm) and Au (50 nm) as the metal contacts. After liftoff, the as-made device was wire bonded onto a leaded chip carrier (LCC) and loaded in the custom-designed high vacuum system (10⁻⁸ mbar) for *in-situ* electrical measurements.

Raman characterization: The Raman measurements were performed by using a WITec Alpha 300R confocal Raman microscope with a single-mode solid-state laser (532 nm) under ambient environment. The power of laser was kept less than 500 μ W to avoid damage of the samples.

In-situ device characterization: Device characterization for the [RuCp*(mes)]₂ modified bilayer WSe₂ FET was carried out in a custom-designed high vacuum system with optoelectronic measurements function and in-situ thin film growth capabilities. The electrical signals were collected by an Agilent 2912A source measure unit at room temperature [45]. [RuCp*(mes)]₂ molecules (synthesized as previously described [37]) were sublimed from a Knudsen cell onto the device. The nominal thickness of deposited molecules was monitored by a quartz crystal microbalance exactly located in front of the sample stage. After dopant deposition, high purity nitrogen and oxygen (>99.99%) were introduced into the chamber for the stability test respectively.

In-situ PES characterization: In-situ PES investigations were carried out in a home-built ultrahigh vacuum system (10^{-10} mbar) at room temperature. The excitation source for UPS and XPS measurement were He I α (hv = 21.2 eV) and Al K α (hv = 1486.7 eV), respectively. Vacuum level shifts were determined from the low kinetic energy part of UPS spectra with a -5 V sample bias. The sample work function ϕ was obtained by the equation ϕ = hv - W, where W is the spectrum width (the energy difference between Fermi level and second electron cut off). The ϕ of the electron analyzer was measured to be 4.30 \pm 0.05 eV. [RuCp*(mes)]₂ molecules were thermally evaporated from a Knudsen cell onto the substrate. The nominal thickness of deposited molecules was monitored by a quartz crystal microbalance exactly located in front of the sample stage and further calibrated by the attenuation of substrate core level peak intensity.

Computation methods: All calculations were performed with the Vienna ab initio Simulation Package (VASP) [46-48]. The generalized gradient approximation (GGA) with the functional described by Perdew-Burke-Ernzerhof (PBE) functional was used

[49]. The projector-augmented wave (PAW) method was applied to describe the wavefunctions in the core regions [50], while the valence wavefunctions were expanded as linear combination of plane-waves with a cutoff energy of 450 eV. In the geometry optimization, the total energy was converged to 10^{-5} eV and the Hellmann-Feynman force on each relaxed atom was less than 0.02 eV/Å. The vacuum space between two adjacent sheets was set at least 10 Å to eliminate the interactive effect on each other. The weak Van der Waals interaction between WSe₂ layers is described by dispersion correction PBE+D2 [51,52].

Acknowledgements

R.G., Q.L. and Y. Z. contributed equally to this paper. The authors acknowledge the financial support from the National Key Research and Development Program of China (2017YFA0204800), NSFC grants (21573156, 21525311, 21773027, 21703032 and 21872100), Natural Science Foundation of Jiangsu Province BK20170005, Singapore MOE Grant R143-000-652-112 and R143-000-A43-114, the US National Science Foundation (DMR-1305247 and DMR-1807797), as well as the technical support from Centre for Advanced 2D Materials for the device fabrication. The authors are thankful for the computational resources at the SEU and National Supercomputing Center in Tianjin.

Data Availability

The raw/processed data required to reproduce these findings cannot be shared at this time as the data also forms part of an ongoing study.

References

- [1] Mak, K. F., et al., Nat. Nanotechnol. (2012) 7 (8), 494
- [2] Ross, J. S., et al., Nat. Nanotechnol. (2014) 9 (4), 268
- [3] Wang, Q. H., et al., Nat. Nanotechnol. (2012) 7 (11), 699
- [4] Lopez-Sanchez, O., et al., Nat. Nanotechnol. (2013) 8 (7), 497
- [5] Liu, Y., et al., Nature (2018), 1
- [6] Kappera, R., et al., Nat. Mater. (2014) 13 (12), 1128
- [7] Schottky, W., Z. Phys. (1939) 113 (5-6), 367
- [8] Mott, N. F., Proc. R. Soc. Lond. A (1939) 171 (944), 27
- [9] Tung, R. T., Appl. Phys. Rev. (2014) 1 (1), 011304
- [10] Bardeen, J., Phys. Rev. (1947) 71 (10), 717
- [11] Gong, C., et al., Nano Lett. (2014) 14 (4), 1714
- [12] Tung, R. T., Phys. Rev. Lett. (2000) 84 (26), 6078
- [13] Kang, J., et al., Phys. Rev. X (2014) 4 (3), 031005
- [14] Cui, X., et al., Nat. Nanotechnol. (2015) 10 (6), 534
- [15] Yu, L., et al., Nano Lett. (2014) 14 (6), 3055
- [16] Liu, Y., et al., Nano Lett. (2015) 15 (5), 3030
- [17] Cho, S., et al., Science (2015) 349 (6248), 625
- [18] Zhu, J., et al., J. Am. Chem. Soc. (2017) 139 (30), 10216
- [19] Chen, W., et al., Prog. Surf. Sci. (2009) 84 (9-10), 279
- [20] Liu, X., et al., Adv. Mater. (2016) 28 (12), 2345
- [21] Laskar, M. R., et al., Appl. Phys. Lett. (2014) 104 (9), 092104
- [22] Hu, Z., et al., Chem. Soc. Rev. (2018) 47 (9), 3100
- [23] Fang, H., et al., Nano Lett. (2013) 13 (5), 1991
- [24] Lei, B., et al., ACS Nano (2018) 12 (2), 2070
- [25] Zhang, X., et al., Adv. Mater. (2016) 28 (47), 10409
- [26] Naab, B. D., et al., Adv. Mater. (2014) 26 (25), 4268
- [27] Kiriya, D., et al., J. Am. Chem. Soc. (2014) 136 (22), 7853
- [28] Lv, R., and Terrones, M., Mater. Lett. (2012) 78, 209
- [29] Wei, P., et al., J. Am. Chem. Soc. (2010) 132 (26), 8852
- [30] Tarasov, A., et al., Adv. Mater. (2015) 27 (7), 1175

- [31] Lin, X., et al., Nat. Mater. (2017) 16 (12), 1209
- [32] Tsai, M.-Y., et al., Chem. Mater. (2017) 29 (17), 7296
- [33] Guo, S., et al., Adv. Mater. (2012) 24 (5), 699
- [34] Geier, M. L., et al., Nano Lett. (2016) 16 (7), 4329
- [35] Paniagua, S. A., et al., Mater. Horiz. (2014) 1 (1), 111
- [36] Zhang, S., et al., Adv. Mater. (2018) 30 (36), 1802991
- [37] Mohapatra, S. K., et al., Chem. Eur. J. (2014) 20 (47), 15385
- [38] Zhao, W., et al., Nanoscale (2013) 5 (20), 9677
- [39] Li, H., et al., Small (2013) 9 (11), 1974
- [40] Olthof, S., et al., Phys. Rev. Lett. (2012) 109 (17), 176601
- [41] Zhou, C., et al., Adv. Funct. Mater. (2016) 26 (23), 4223
- [42] Giordano, A. J., et al., ACS Appl. Mater. Interfaces (2015) 7 (7), 4320
- [43] Schlesinger, R., et al., Nat. Commun. (2015) 6
- [44] Casu, M. B., et al., Adv. Mater. (2010) 22 (33), 3740
- [45] Xiang, D., et al., Nat. Commun. (2015) 6, 6485
- [46] Kresse, G., and Hafner, J., Phys. Rev. B (1993) 48 (17), 13115
- [47] Kresse, G., and Furthmüller, J., Phys. Rev. B (1996) 54 (16), 11169
- [48] Kresse, G., and Furthmüller, J., Comput. Mater. Sci. (1996) 6 (1), 15
- [49] Perdew, J. P., et al., Phys. Rev. Lett (1996) 77, 3865
- [50] Kresse, G., and Joubert, D., Phys. Rev. B (1999) 59 (3), 1758
- [51] Grimme, S., J. Comput. Chem. (2006) 27 (15), 1787
- [52] Grimme, S., et al., J. Chem. Phys. (2010) 132 (15), 154104

Supporting Information

Degenerate Electron-Doping in Two-dimensional Tungsten
Diselenide with a Dimeric Organometallic Reductant

Rui Guo¹, Qiang Li², Yue Zheng^{3,4}, Bo Lei^{3,4}, Haicheng Sun¹, Zehua Hu^{3,4}, Jialin Zhang^{1,3}, Li Wang⁵, Elena Longhi⁶, Stephen Barlow⁶, Seth R. Marder⁶, Jinlan Wang^{2,7}, Wei Chen^{1,3,8,9}

⁶Center for Organic Photonics and Electronics and School of Chemistry and Biochemistry, Georgia Institute of Technology, Atlanta, Georgia 30332, USA

⁷Synergetic Innovation Center for Quantum Effects and Applications (SICQEA), Hunan Normal University, Changsha, 410081, P.R. China

⁷Synergetic Innovation Center for Quantum Effects and Applications (SICQEA), Hunan Normal University, Changsha, 410081, P.R. China

⁸National University of Singapore (Suzhou) Research Institute, Suzhou, 215123, P.R. China

⁹Joint School of National University of Singapore and Tianjin University, International Campus of Tianjin University, Binhai New City, Fuzhou, 350207, P. R. China

*E-mail: jlwang@seu.edu.cn (JL Wang)

*E-mail: phycw@nus.edu.sg (W Chen)

The bilayer nature of WSe₂ flake configured for device in Figure 2b, 2c and 2d is confirmed by various characterizations. The Raman fingerprint for monolayer WSe₂ is

¹Department of Chemistry, National University of Singapore, 117543, Singapore

²School of Physics, Southeast University, Nanjing, 211189, P.R. China

³Department of Physics, National University of Singapore, 117542, Singapore

⁴Center for advanced 2D materials, National University of Singapore, 117546, Singapore

⁵Institute for Advanced Study and Department of Physics, Nanchang University, Nanchang, 330031, P.R. China

the absence of peak at ~308 cm⁻¹, while for bi- and tri-layer, the main difference is the Raman peak intensity [1]. As it is hard to show the intensity difference in only one spectrum, the bilayer nature of the sample was checked through the combination with AFM line profile measurement. The height of the flake is roughly 1.4 nm, corresponding to two layers of WSe₂. In addition, the photoluminescence spectrum of the same sample is given in Figure S1, which clearly displays a negatively charged trion peak (~1.54 eV) and a neutral exciton peak (~1.64eV). The well agreement of this spectrum with previous reported photoluminescence spectrum of bilayer WSe₂ [2] further corroborates the bilayer nature of our sample.

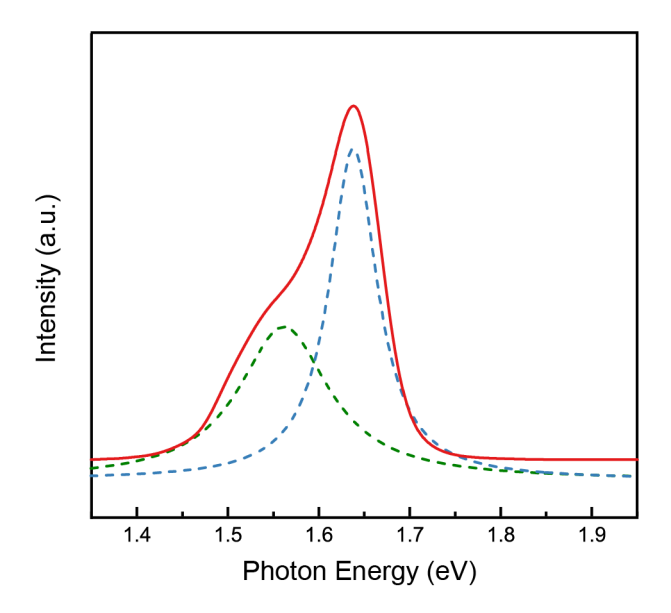


Figure S1. Photoluminescence spectrum of the bilayer WSe₂ under 532nm excitation.

Both electron mobility μ_e and concentration N_e (at certain gate voltage V_g) are calculated from the linear regime in the transfer curve of WSe₂ FET in Figure 2b. The electron mobility μ_e are extracted by the formula $\mu_e = \frac{L}{WC_iV_{sd}} \frac{dI_{sd}}{dV_g}$, where dI_{sd}/dV_g equals to the slope of the linear region of the electron side in the transfer curve, L and W are length and width of the conduction channel, respectively, C_i is the capacitance per unit area between WSe₂ and the back gate (*i.e.*, the capacitance per unit area of the dielectric SiO₂ layer and thus given by $C_i = \frac{\varepsilon_0 \varepsilon_r}{d}$, ε_0 , ε_r and d are dielectric constant of vacuum, dielectric constant of SiO₂ and thickness of SiO₂, respectively), V_{sd} is the source-drain bias. The electron

concentration N_e at certain gate volatage V_g is calculated by the equation $N_e = -C_i \frac{(V_g - V_{th})}{e}$, where V_{th} is determined by extrapolating the current onset of the linear region of the electron side in the transfer curve.

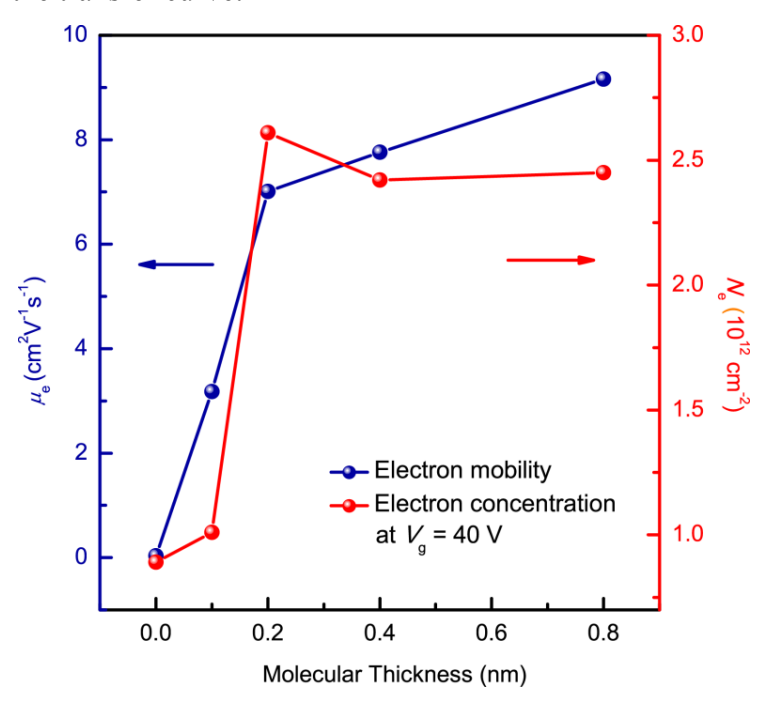


Figure S2. Extracted electron mobility and electron concentration at $V_g = 40 \text{ V}$ of WSe₂ FET device plotted against molecular thickness.

In our manuscript, the bilayer WSe₂ device is discussed thoroughly as a representative example of 2D WSe₂ device. The weakened gate dependence, *i.e*, the linear transport curve in logarithmic scale and great enhancement of electric conductance with molecular donor functionalization are observed on all the measured devices, thickness varying from monolayer to four-layer. For monolayer WSe₂ device (Figure 2e and 2f), we observed similar evolution of electrical transport properties during the deposition process. The Raman spectrum and optical image are presented in Figure S3 to confirm the monolayer nature of WSe₂.

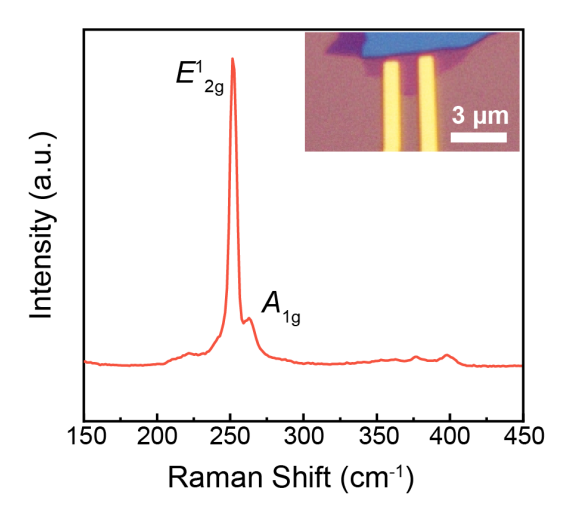


Figure S3. Raman spectrum of the monolayer WSe₂ FET functionalized with [RuCp*(mes)]₂. The absence of peak at ~308 cm⁻¹ in Raman spectrum confirms the monolayer nature of WSe₂ flake. Insert: optical image of the device.

Theoretical calculations reveal that interaction between molecule and WSe₂ is confined at interface; the presence of extra bottom layer in bilayer WSe₂ has no apparent effect on the interfacial charge transfer as well as the evolution of energetic structure of WSe₂ after the molecular functionalization (Figure 5 and Figure S11).

Compared with monolayer, it is more feasible to prepare bilayer WSe₂ device with larger size. Transport behavior of another bilayer WSe₂ is given in Figure S4.

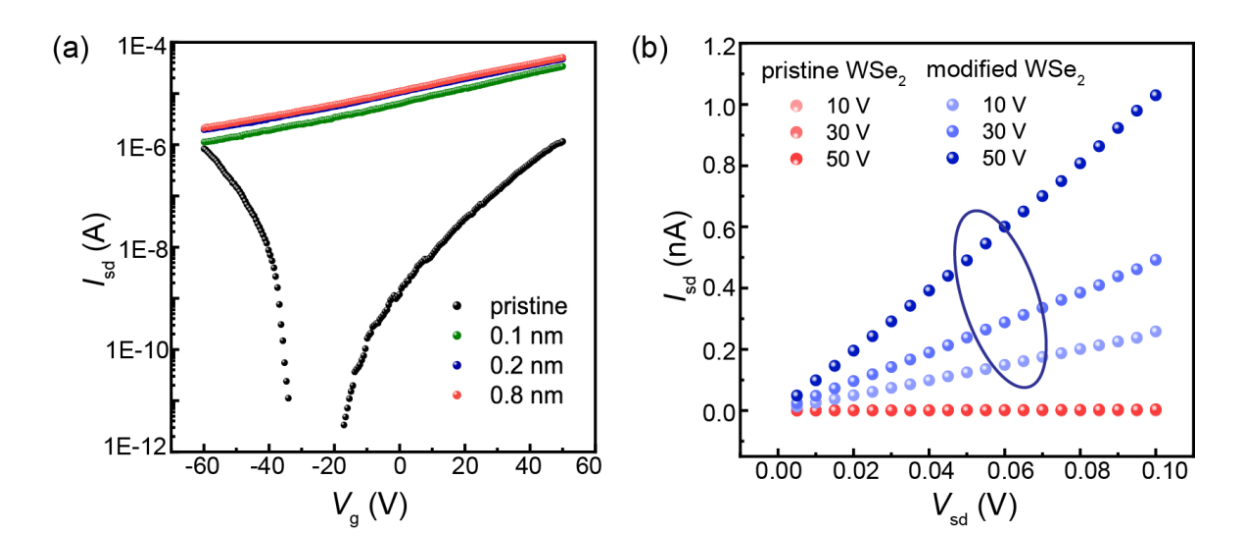


Figure S4. Characteristic of another typical WSe₂ device modified by [RuCp*(mes)]₂.

Because the electronic property of WSe₂ is thickness dependent and also varies from device to device, in Figure S5 we draw the statistic distribution of electrical conductance enhancement $G_{\rm m}/G_{\rm p}$ among all the six WSe₂ devices measured with thickness varying from monolayer to four-layer, where $G_{\rm m}$ is the conductance of modified WSe₂ device and $G_{\rm p}$ is the conductance of pristine device. It is clear that on average, the functionalization of WSe₂ by molecular donor can improve the conductance by five orders of magnitude.

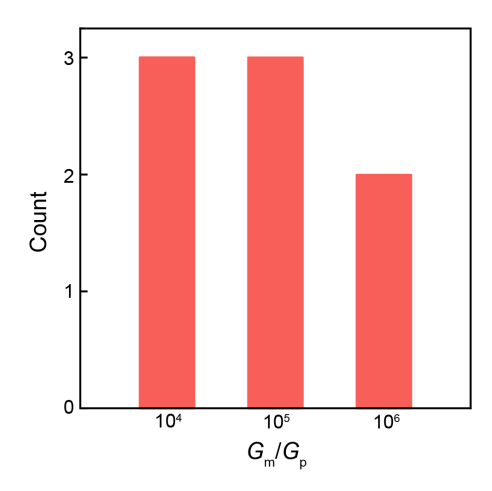


Figure S5. Count of the WSe₂ devices with corresponding conductance enhancement.

We also carry out device measurements for the pristine and modified WSe₂ FET under varying temperatures to extract SB heights. The transfer curves of the device are shown in Figure S6 (a), which is similar to the results demonstrated before. The SB heights $\Phi_{\rm B}$ are calculated based on the thermionic emission equation corrected for 2D transport channel [3-5],

$$I_{\rm sd} = AA_{2D}^* T^{3/2} \exp\left[-\frac{q}{k_{\rm B}T}(\Phi_{\rm B} - \frac{V_{\rm sd}}{n})\right],$$
 (1)

where A is the contact area, A_{2D}^* is the two-dimensional equivalent Richardson constant, T is the temperature, q is the elementary electron charge, $k_{\rm B}$ is the Boltzmann constant and n is the ideality factor. Under certain $V_{\rm sd}$, $\ln{(I_{\rm sd}/T^{3/2})}$ plotted against 1000/T would be linear and a slope S can be extracted. Here a typical Arrhenius plot of $\ln{(I_{\rm sd}/T^{3/2})}$ vs 1000/T for the pristine WSe₂ device with $V_{\rm g} = 50$ V was presented in Figure S6 (b). The subsequent linear extrapolation of the y-axis intercept of S vs $V_{\rm sd}$ yields $S_0 = -\frac{q\Phi_B}{1000k_B}$, as shown in Figure S6 (c). A comparison of $\Phi_{\rm B}$ in WSe₂ device before and after the

modification of 0.4 nm molecular donor was shown in Figure S6 (d). It is obvious that after the functionalization with $[RuCp^*(mes)]_2$ molecules, the Φ_B at WSe₂/metal interface is largely reduced. For example, when $V_g = 50V$, Φ_B for pristine WSe₂ device is 66.5 meV while for modified WSe₂ device is only 15.2 meV. A reduction of ~80% can be deduced.

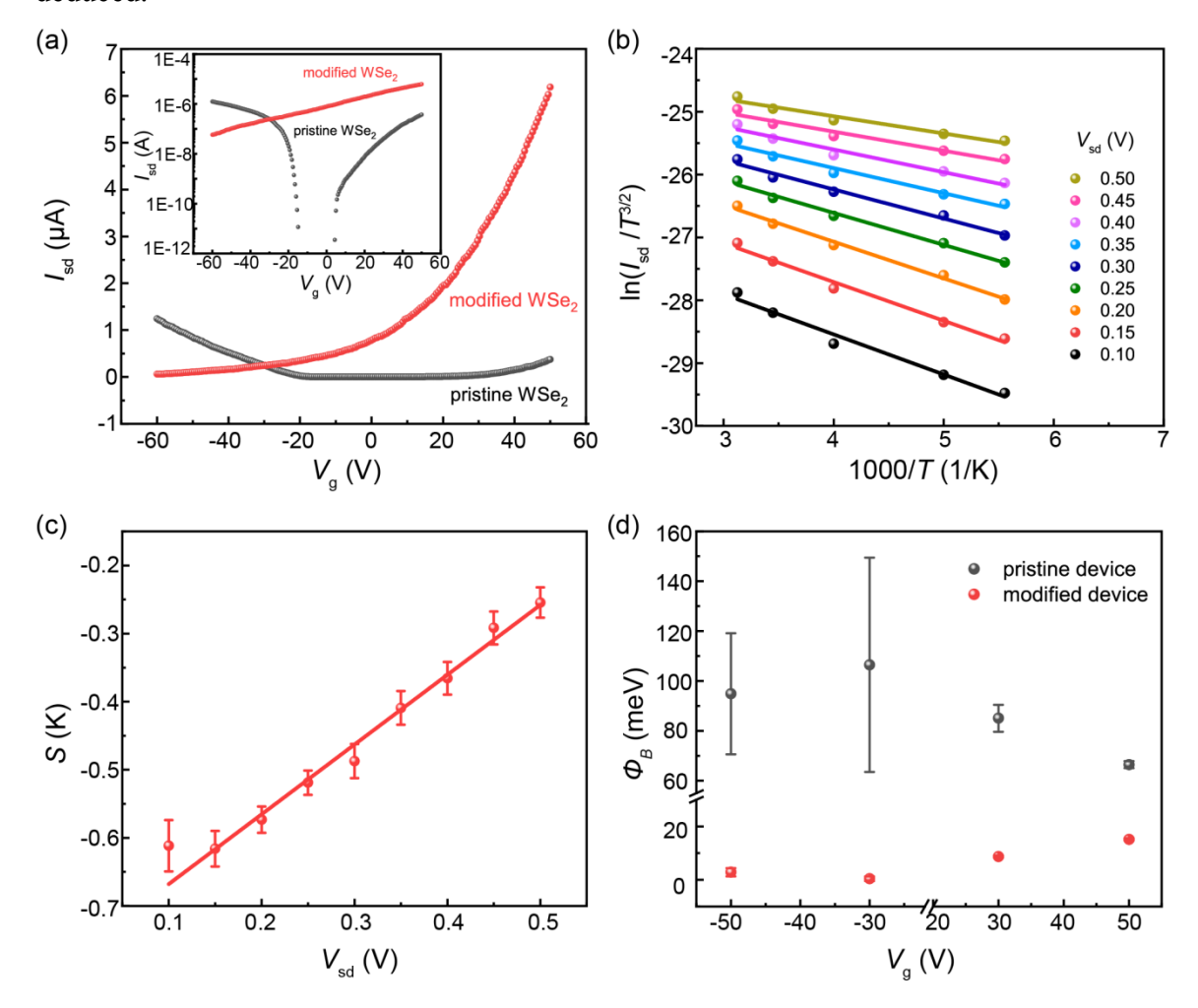


Figure S6. Comparison of SB heights for pristine and modified WSe₂ FET device. (a) The transfer curve of the WSe₂ device before and after modification (0.4 nm molecular donor) for SBH calculation, $V_{\rm sd} = 1$ V. Insert: Logarithmic plot of the transfer curves. (b) Linear fit of the Arrhenius plot, $\ln(I_{\rm sd}/T^{3/2})$ vs 1000/T, for pristine WSe₂ device with $V_{\rm g} = 50$ V. (c) Slope extracted from (b) as a function of $V_{\rm sd}$. $\Phi_{\rm B}$ is derived from the y-intercept. (d) Comparison of SBH for pristine and modified WSe₂ device under different gate voltage.

In-situ Raman and PL spectra collected from monolayer WSe₂ before and after the molecule deposition are shown in Figure S7 and S8, respectively.

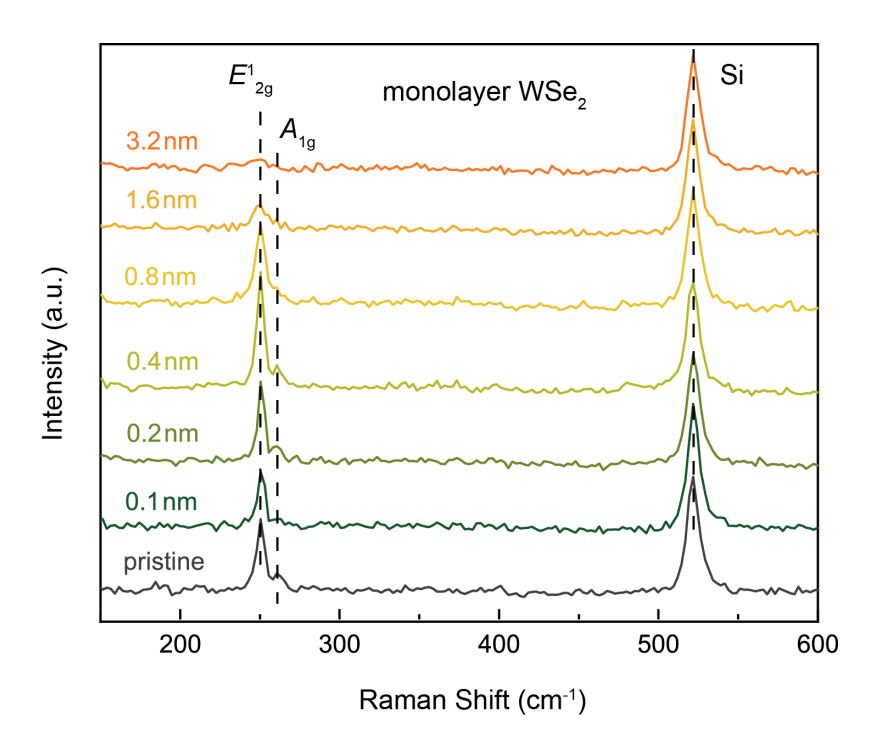


Figure S7. The compassion of Raman spectra collected from monolayer WSe₂ with nominal molecular thickness increasing from 0 to 3.2 nm.

In addition to the quenching of overall PL intensity with increasing amount of molecules, further analysis of the PL spectra gives out two components, the negatively charged trion peak at 1.65 eV and exciton peak at 1.67 eV (Figure S8 (b)). The intensity of trion/exciton (It/Ie) is 0.58. After the deposition of 0.4 nm molecule, the trion peak shifts to 1.62 eV while the exciton peak almost remains in the same position. The ratio It/Ie increases to 0.67, suggesting a higher weight of the trion peak.

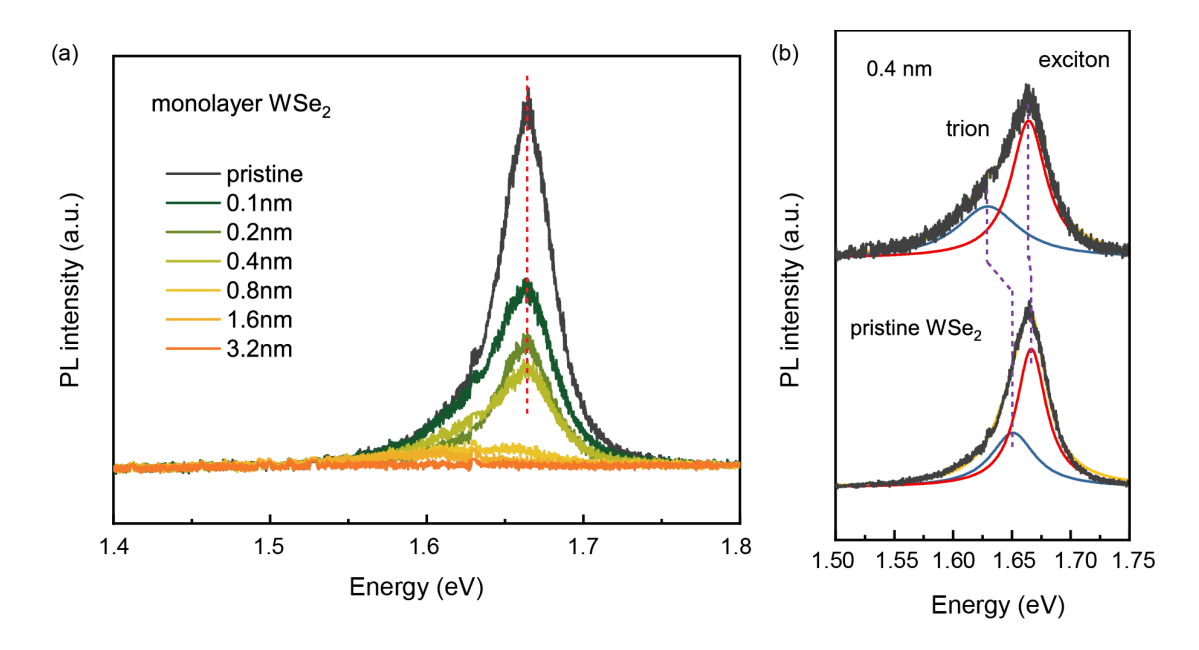


Figure S8. (a) Evolution of PL spectra on monolayer WSe₂ before and after the deposition of molecule. (b) Peak fitting results of PL spectra on pristine WSe₂ (bottom) and that with 0.4 nm molecular dopants (top).

Core level spectra of W 4f and Se 3d show no new peak (Figure S9), and therefore exclude the possibility of chemical bond formation between WSe₂ and [RuCp*(mes)]₂. The spectra shape of W and Se photoemission lines with molecule functionalization are identical to those of the pristine substrate, indicating that the modification does not chemically alter the host structure.

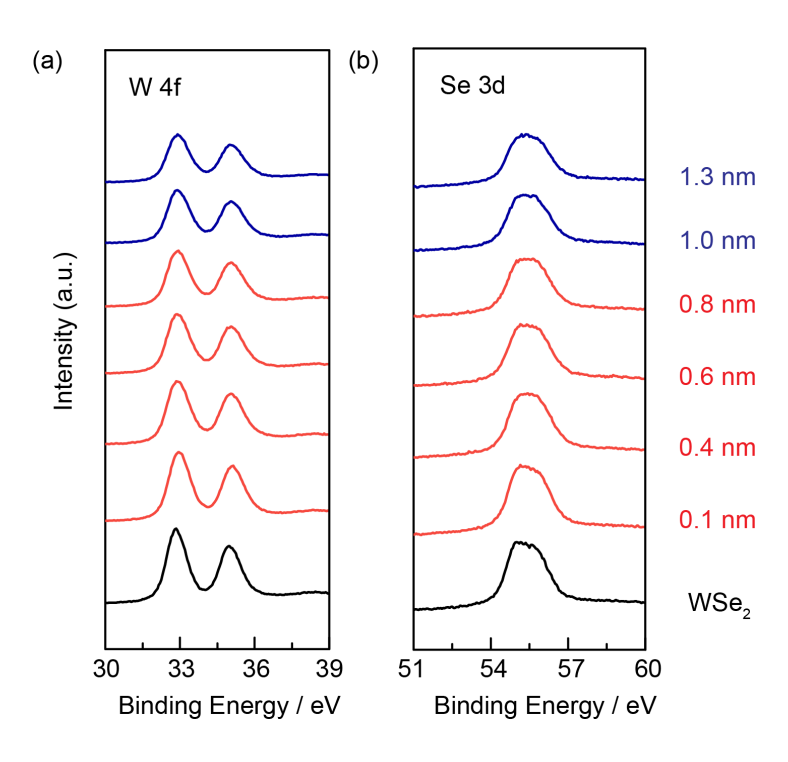


Figure S9. Core level spectra of (a) W 4f and (b) Se 3d evolution during [RuCp*(mes)]₂ deposited on WSe₂.

Similar to Figure 4a, the modified device demonstrates great stability in N_2 as the transfer curves after exposure almost resembles that before exposure with negligible drop of source-drain current (Figure S10a). However, when exposing the doped system to air, the source-drain current at high positive gate voltage still maintains but the negative gate voltage side quickly drops (Figure S10b). The transfer curve loses degenerate characteristic and the device begins to behave like a strong n-type semiconductor. As the humidity of indoor air in Singapore is around $60 \sim 80\%$, we assume water plays an important role in this degradation mechanism. Further investigations are required to thoroughly clarify this issue.

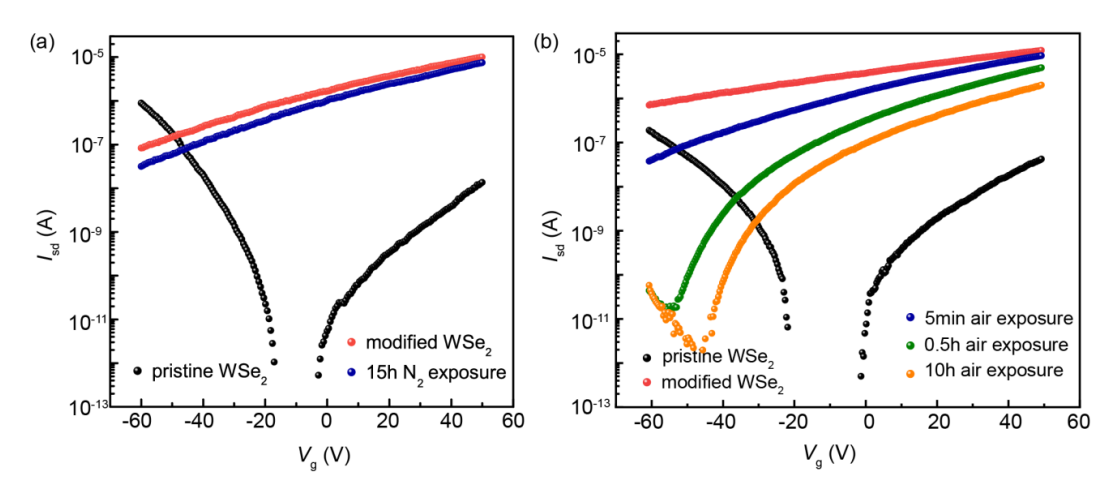


Figure S10. Stability investigation of the bilayer WSe₂ FET functionalized [RuCp*(mes)]₂. The comparison of transfer curves in logarithmic scale at $V_{\rm sd} = 1$ V of the pristine WSe₂ device, the same device modified by [RuCp*(mes)]₂ and then *in-situ* exposed to (a) N₂ for 15h and (b) air for 5min, 0.5h, and 3h, respectively.

[RuCp*(mes)] monomer, as a strong electron donor species, transfers electrons to WSe₂ effectively, resulting in the partial occupation of conduction bands around M-K point in bilayer WSe₂ (Figure S11). As a consequence, numbers of conduction bands cross over the Fermi level, rendering the [RuCp*(mes)]-WSe₂ complex demonstrate metallic-like transport behavior.

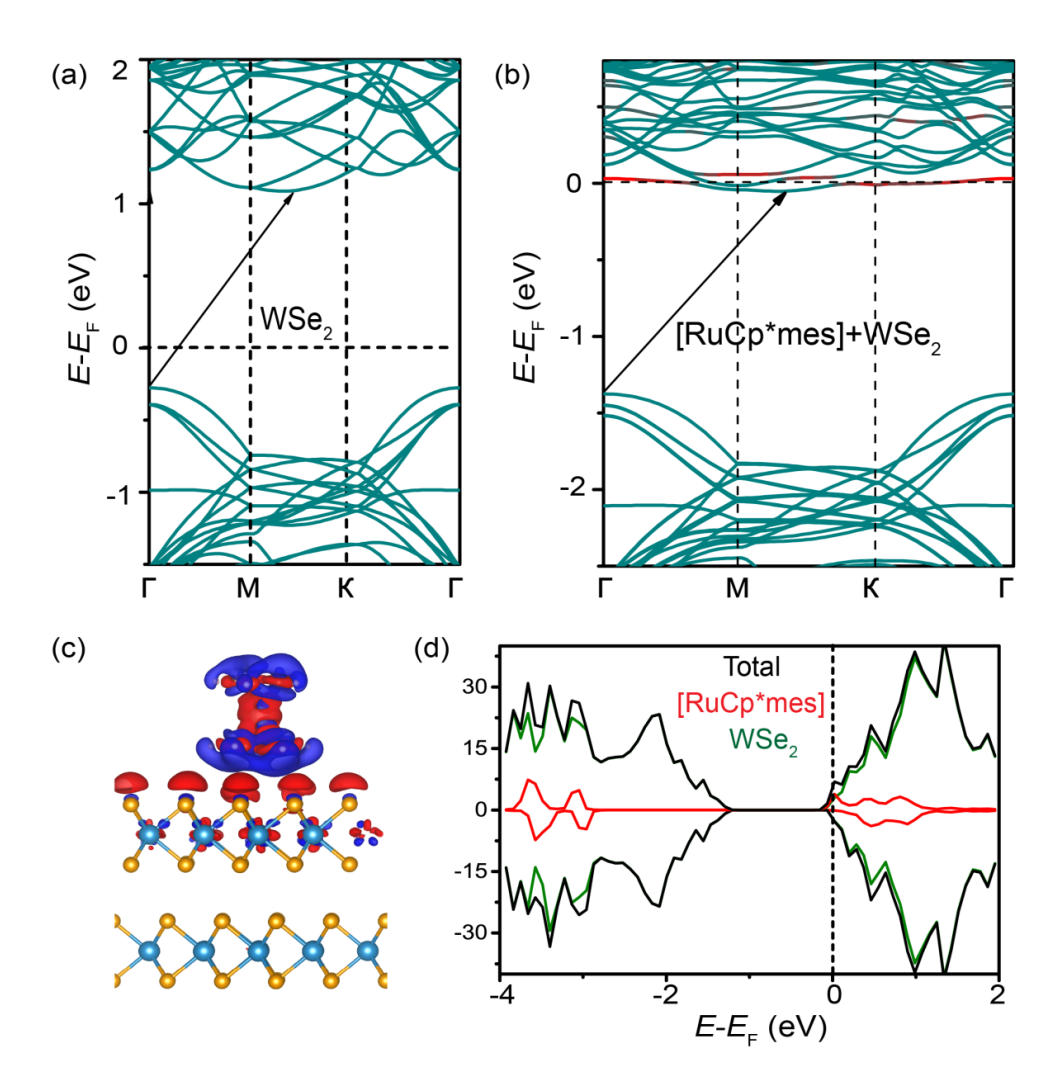


Figure S11. Band structures of (a) pristine bilayer WSe₂ and (b) one [RuCp*(mes)] monomer decorated bilayer WSe₂. The Fermi level is set to zero. (c) Charge density difference between [RuCp*(mes)]-bilayer WSe₂ and isolated components. Red and blue colors represent charge accumulation and depletion region, respectively. (d) DOS of the [RuCp*(mes)]-bilayer WSe₂ system.

The adsorption energy is calculated by $E(ads) = [E(MO@WSe_2) - E(MO) - E(WSe_2)]/n$, where MO denotes [RuCp*(mes)] and n is the number of interacting atoms. As seen in Figure 5 and Figure S11, one of the carbocyclic rings interacts with the substrate in a flat configuration, and the adsorption energy is thus calculated as -0.23 eV.

The interaction between [RuCp*(mes)] and monolayer WSe₂ surface was also calculated by two other dispersion correction methods, PBE+D3 and optPBE-vdW, respectively. As

shown in Figure S12, all three methods including PBE+D2 used in the main context show very similar electronic properties, such as band gaps and band dispersions, especially those around Fermi level. The adoption of different dispersion correction methods therefore has no significant influence in analyzing the electronic properties of the hybrid system.

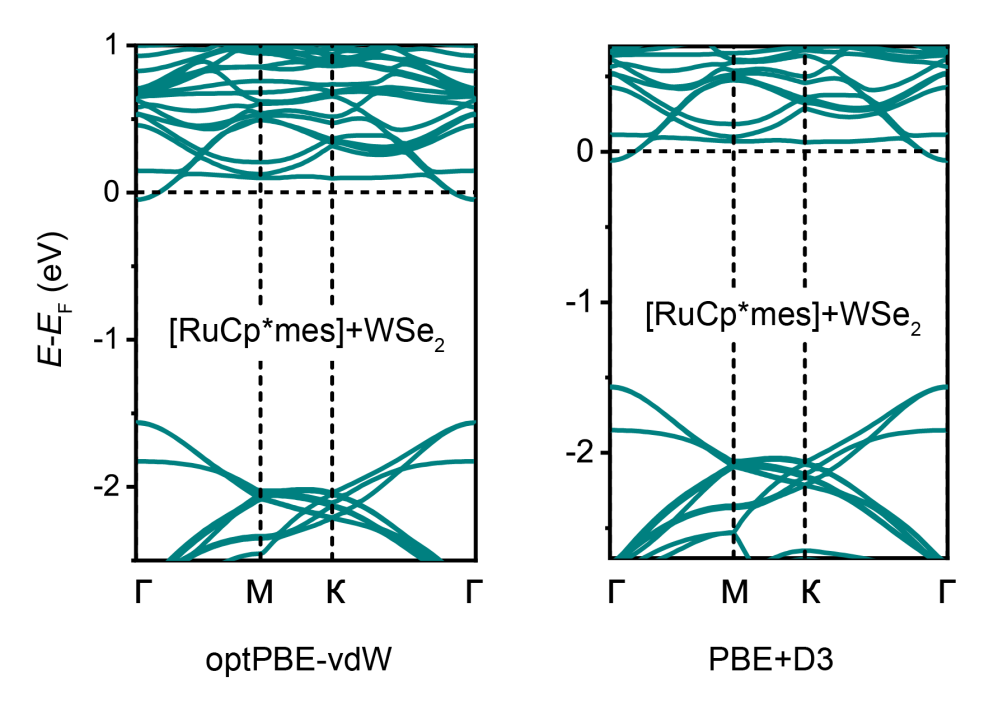


Figure S12. Band structures of one [RuCp*(mes)] monomer decorated monolayer WSe₂ calculated by two dispersion correction methods, optPBE-vdW (left) and PBE+D3 (right), respectively.

References

- [1] Li, H., et al., Small (2013) 9 (11), 1974
- [2] Zeng, H., et al., Sci. Rep. (2013) 3, 1608
- [3] Anwar, A., et al., J. Appl. Phys. (1999) 85 (5), 2663
- [4] Chen, J.-R., et al., Nano Lett. (2013) 13 (7), 3106
- [5] Zhou, Y., et al., Appl. Phys. Lett. (2010) 96 (10), 102103